Reflection Coefficient Stability Criterion for Multi-Bus Multi-VSC Power Systems

Chou, Shih Feng; Wang, Xiongfei; Blaabjerg, Frede

Published in:
IEEE Access

DOI (link to publication from Publisher):
10.1109/ACCESS.2020.3002661

Publication date:
2020

Document Version
Publisher's PDF, also known as Version of record

IEEE Access
Multidisciplinary | Rapid Review | Open Access Journal

Received May 18, 2020, accepted June 11, 2020, date of publication June 15, 2020, date of current version June 25, 2020.

Digital Object Identifier 10.1109/ACCESS.2020.3002661

Reflection Coefficient Stability Criterion for Multi-Bus Multi-VSC Power Systems

SHIH-FENG CHOU, (Member, IEEE), XIONGFEI WANG, (Senior Member, IEEE), AND FREDE BLAABJERG, (Fellow, IEEE)
Department of Energy Technology, Aalborg University, 9220 Aalborg, Denmark

Corresponding author: Shih-Feng Chou (shc@et.aau.dk)

This work was supported by the Reliable Power Electronic-Based Power System (REPEPS) project at the Department of Energy Technology, Aalborg University, as a part of the Villum Investigator Program funded by the Villum Foundation.

ABSTRACT This paper proposes a reflection coefficient stability criterion for multi-bus power systems with multiple voltage-source converters (VSCs). In the method, VSCs are modeled as two-port networks, which are then characterized by the incident and reflected power waves, as well as their ratios, i.e. reflection coefficients. Two superior features over the impedance-based stability analysis are provided, which are no need for system partitioning to avoid unstable subsystems, and the identification of relative stability and the critically oscillating frequency at each bus of the power system. Case studies with experimental results demonstrate the effectiveness of the approach.

INDEX TERMS Reflection coefficient, scattering parameters, stability analysis, two-port network, voltage source converters.

I. INTRODUCTION

In modern power systems, the voltage-source converters (VSCs) are increasingly used as the interfacing converters in renewable energy resources (e.g., solor and wind energy). This results in an increase of the penetration level of power electronics in power grids. The multi-timescale control dynamics of VSCs interact not only with the grid but also with the adjacent VSCs, which may cause resonances over a wide frequency range, jeopardizing the grid stability [1], [2].

The impedance-based stability analysis methods are widely used to evaluate the system stability in the frequency domain. There exist two kinds of resonances below the Nyquist frequency of the control systems of VSCs [3], which are the harmonic resonances and sideband resonances of the fundamental frequency. The harmonic resonances are primarily caused by the inner current loop control with symmetric dynamics in the dq- or $\alpha\beta$-frame. Thus, the system can be modeled as two single-input single-output (SISO) transfer functions or one complex transfer function, and then the stability is analyzed using the Nyquist stability criterion. In contrast, the cause of sideband resonances of the fundamental frequency is the asymmetrical dynamics in the dq-frame, e.g., phase-locked loop (PLL) [4]–[9], and the other power control loops [10]–[12], which are not able to be characterized as SISO transfer functions [13]. Only the multiple-input multiple-output (MIMO) transfer function matrices can capture these frequency-coupling dynamics [8]–[10].

The MIMO impedance matrix modeling methods have been developed either in the dq-frame [4]–[6], [11] or in the $\alpha\beta$-frame [7]–[10], and the mathematical relationships between these two reference-frame impedance matrices have been elaborated in [8]. The main difference between these two impedance matrices is that the dynamic coupling between different frequencies in the phase domain are hidden in the dq-frame [4]–[6], but are directly revealed in the $\alpha\beta$-frame [3], [8], [9]. Yet, the generalized Nyquist criterion is inevitably used to analyze the stability of such MIMO systems, which hardly provides a design-oriented analysis, due to the lack of explicit stability margin definitions.

In [14], to avoid using the generalized Nyquist stability criterion and describe the MIMO system with SISO transfer functions, the grid-connected VSC has been considered as a two-port network using admittance parameters (Y-parameters), and then this common SISO open-loop gain of the MIMO system is directly derived from the MIMO impedance matrices of the VSC and grid impedance. The common SISO open-loop gain is further translated into two SISO admittance ratios at each port. Thus, by deriving the

The associate editor coordinating the review of this manuscript and approving it for publication was Md. Rabiul Islam.

corresponding SISO Thévenin equivalent circuits, the stability at each port of the two-port network can be analyzed separately using the impedance-ratio stability criterion, where the conventional stability analysis tools, e.g. Bode plot and Nyquist plot, can then be used. However, when using the Nyquist stability criterion, the prior knowledge of the number of open-loop right-half-plane (RHP) poles in the impedance-ratio is required. To avoid the influence of the open-loop RHP poles in the impedance-based analysis, an impedance-sum stability analysis method has been proposed by analyzing the closed-loop characteristic equation based on Cauchy's argument principle requiring the subsystem to be stable individually [15].

For multi-VSC, multi-bus power systems, an impedance-ratio based analysis method considering the open-loop RHP poles has been presented for multi-prallel VSCs, which analyzes the system using the Nyquist stability criterion for multi-loop dynamic systems. Yet, the system needs to be partitioned into multiple $Z+Z$ or $Z+Y$ subsystems to perform the stability analysis [16]. On the other hand, the impedance-sum based analysis method has been developed in the wind power system for analyzing the stability at a specified bus by partitioning the system into the corresponding impedance network model [17]. Both methods require the prior knowledge of the system in order to properly partition the system into subsystems.

Alternatively, our recent work [18] has found that using the scattering parameters (S-parameters) and the reflection coefficients to analyze multi-bus, multi-VSC power system does not need to partition the system. The S-parameters and reflection coefficients are based on the two-port network analysis, which are generally used to analyze the system with a large number of component connections in the radio frequency (RF) engineering [19]. Further, in the method of [18], only the reflection coefficients on both sides of the specific bus are needed to obtain the SISO open-loop gain, which facilitates a more efficient modeling and analysis, and this method has been first put in practice in our other work for the multi-bus, multi-VSC power system [20].

In this paper, a SISO reflection coefficient stability criterion is proposed, where the obtained SISO open-loop gain with reflection coefficients, which was introduced in [18], is further proven as unaffected by the open-loop RHP poles of the impedances. Therefore, the system partitioning in order to make the subsystem stable is unnecessary, and it can still provide the relative stability even for the MIMO dynamic systems of VSCs. Moreover, the stability analysis procedure, which was briefed in [20], is established systematically in 6 steps. Based on the proposed reflection coefficient stability criterion, the sensitive bus in the multi-bus, multi-VSC power system can be localized. The resonance condition of the sensitive bus and the critically oscillating frequency can be distinctly identified. Experimental results and theoretical analysis in case studies verify the effectiveness of the stability analysis procedure and the stability criterion.

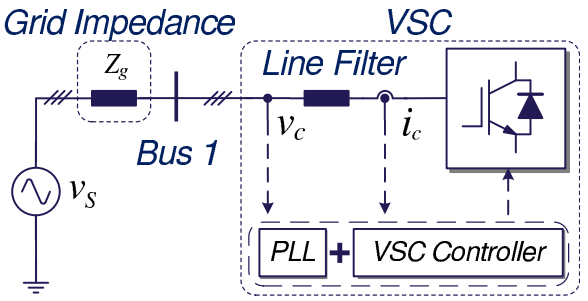

FIGURE 1. Single-line diagram and system configuration of single grid-connected VSC.

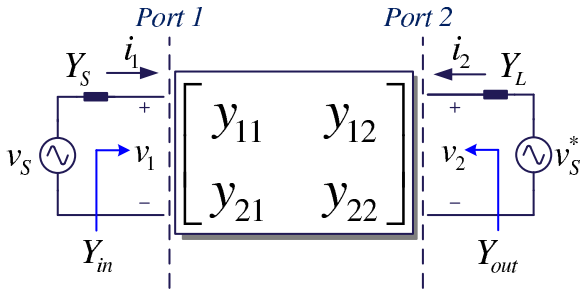

FIGURE 2. Two-port network of grid-connected VSC using Y-parameter.

II. TWO-PORT NETWORK MODELING METHODS OF SINGLE GRID-CONNECTED VSC

In this section, the use of two-port network with Y-parameters for analyzing the stability of grid-connected VSC is introduced first, which utilizes the impedance-ratio stability criterion for evaluation [14]. Then, the two-port network modeling method using the S-parameters and reflection coefficients is introduced in the same system.

A. TWO-PORT NETWORK MODELING METHOD USING Y-PARAMETER

Fig. 1 illustrates the system configuration of grid-connected VSC connected to an infinite bus voltage v_S with a grid impedance Z_g, where the line filter current i_c and the voltage at PCC point v_c are the inputs of the phase-locked loop (PLL) and VSC controller. Then, the electrical relationship at the PCC point can be described as the electrical connection between the grid impedance Z_g and the input admittance MIMO matrix of VSC in the $\alpha\beta$-frame [8].

The two-port network modeling of a grid-connected VSC in the admittance form has been elaborated in detail in [14], whose representation is shown in Fig. 2, where the small-signal MIMO admittance model of the VSC is represented with a general linear time-invariant two-port network. The two grid impedance entries of the diagonal grid impedance matrix Z_g and Z_g^* are distributed to two ports of the VSC network and connected to two voltage sources v_S and v_S^*, where Z_g^* is the complex conjugate of Z_g and their admittance representations are given as

$$Y_S = \frac{1}{Z_g} \quad Y_L = \frac{1}{Z_g^*} \tag{1}$$

The electrical port relations of the two-port network in Fig. 2 are given as

$$\begin{bmatrix} i_1 \\ i_2 \end{bmatrix} = \begin{bmatrix} y_{11} & y_{12} \\ y_{21} & y_{22} \end{bmatrix} \begin{bmatrix} v_1 \\ v_2 \end{bmatrix} \tag{2}$$

where the entries in the admittance matrix of (2) are defined under short-circuit operating condition which are shown as

$$\begin{aligned} y_{11} &\triangleq \left.\frac{i_1}{v_1}\right|_{v_2=0} \quad y_{12} \triangleq \left.\frac{i_1}{v_2}\right|_{v_1=0} \\ y_{21} &\triangleq \left.\frac{i_2}{v_1}\right|_{v_2=0} \quad y_{22} \triangleq \left.\frac{i_2}{v_2}\right|_{v_1=0} \end{aligned} \tag{3}$$

By identifying the equivalent input and output admittances, Y_{in} and Y_{out}, of the two-port network, the SISO closed-loop gains of the MIMO system at each ports can be obtained as [14]

$$\frac{v_1}{v_S} = \frac{\dfrac{Y_S}{Y_{in}}}{1+\dfrac{Y_S}{Y_{in}}} \tag{4}$$

$$\frac{v_2}{v_S^*} = \frac{\dfrac{Y_L}{Y_{out}}}{1+\dfrac{Y_L}{Y_{out}}} \tag{5}$$

where the other two complementary SISO closed-loop gains, $\frac{v_2}{v_S}$ and $\frac{v_1}{v_S^*}$, are bounded by the electrical behavior revealed in (2), and thus they share the same denominators as (4) and (5), respectively. Moreover, (4) and (5) provide the conventional closed-loop gain forms, and hence the stability can be analyzed by checking the SISO open-loop gains, $\frac{Y_S}{Y_{in}}$ and $\frac{Y_L}{Y_{out}}$, using the conventional stability analysis tools, e.g., Nyquist plot or Bode plot. The stability analysis method proposed in [14] has clearly used the impedance-ratio stability criterion. Thus, the information of the RHP zero in the denominator is necessary to evaluate stability correctly [15].

It is worth mentioning that the grid-connected VSC has been modeled as a general two-port network, other variants of electrical parameters (Z-, H-, G-, and ABCD-parameters) can also be used to describe the two-port network, and then the mathematically equivalent forms of the closed-loop gains describing the terminal electric relationships can be obtained in a similar way [21]. However, in order to analyze the dynamics using the impedance-ratio stability criterion at a specific bus in a multi-bus power system, the Thévenin's theorem must first be used to obtain two equivalent admittances, and the existence of RHP zeros in the denominator must be identified. Therefore, the difficulty of the entire process increases greatly with the complexity of the system.

B. TWO-PORT NETWORK MODELING METHOD USING S-PARAMETER

To facilitate analysis of a large number of component connections in a network, the S-parameter representation has been introduced for interconnection of RF and Microwave circuits, which does not use the terminal voltage and current but uses the incident and reflected power waves to characterize a two-port network [19].

1) INCIDENT AND REFLECTED POWER WAVES

Kurokawa [22] defined the incident power wave a_i and reflected power wave b_i at i^{th} port for a generic two-port network as

$$a_i = \frac{1}{2}\frac{v_i + Z_i i_i}{\sqrt{Re\{Z_i\}}} \quad b_i = \frac{1}{2}\frac{v_i - Z_i^* i_i}{\sqrt{Re\{Z_i\}}}, \quad i = 1, 2 \tag{6}$$

where Z_i and Z_i^* are the terminated impedance and its complex conjugate for port i. v_i and i_i are the complex number form of the voltage and current at port i. In general, the terminated impedance of each ports is assumed to be identical, and then the incident and reflected power waves are simplified as

$$a_i = \frac{1}{2}\frac{v_i + Z_0 i_i}{\sqrt{Re\{Z_0\}}} \quad b_i = \frac{1}{2}\frac{v_i - Z_0^* i_i}{\sqrt{Re\{Z_0\}}}, \quad i = 1, 2 \tag{7}$$

where Z_0 is called as the characteristic impedance, and the selection of the value of Z_0 will be discussed in Section II-B2. The relationships between the incident, reflected power waves and the S-parameters in a two-port network are given as

$$\begin{bmatrix} b_1 \\ b_2 \end{bmatrix} = \begin{bmatrix} s_{11} & s_{12} \\ s_{21} & s_{22} \end{bmatrix} \begin{bmatrix} a_1 \\ a_2 \end{bmatrix} \tag{8}$$

where

$$\begin{aligned} s_{11} &\triangleq \left.\frac{b_1}{a_1}\right|_{a_2=0} \quad s_{12} \triangleq \left.\frac{b_1}{a_2}\right|_{a_1=0} \\ s_{21} &\triangleq \left.\frac{b_2}{a_1}\right|_{a_2=0} \quad s_{22} \triangleq \left.\frac{b_2}{a_2}\right|_{a_1=0} \end{aligned} \tag{9}$$

Unlike the admittance parameters given in (3), which are defined under short-circuit operating condition, the scattering parameters in (9) are defined under zero incident wave, where the incident waves are the combination of voltage and current at the terminals given in (7). Therefore, the type of power sources is irrelevant to describing network.

2) SELECTION OF THE CHARACTERISTIC IMPEDANCE Z_0

The characteristic impedance in the RF/Microwave field is used to describe the frequency response of the transmission channel, where it is determined by the geometry and materials but is independent on the length of the transmission line [23]. In the power system, the transmission lines are the major contributor to the grid impedances, which has been similarly described with the surge impedance [24]. On the other hand, the input admittances of the grid-connected VSCs vary with the operating conditions or controller parameters. Yet, the transmission line used in the system can be predefined. Therefore, the surge impedance of an uniform transmission line can be selected as the characteristic impedance of the two-port network, which is introduced as follows:

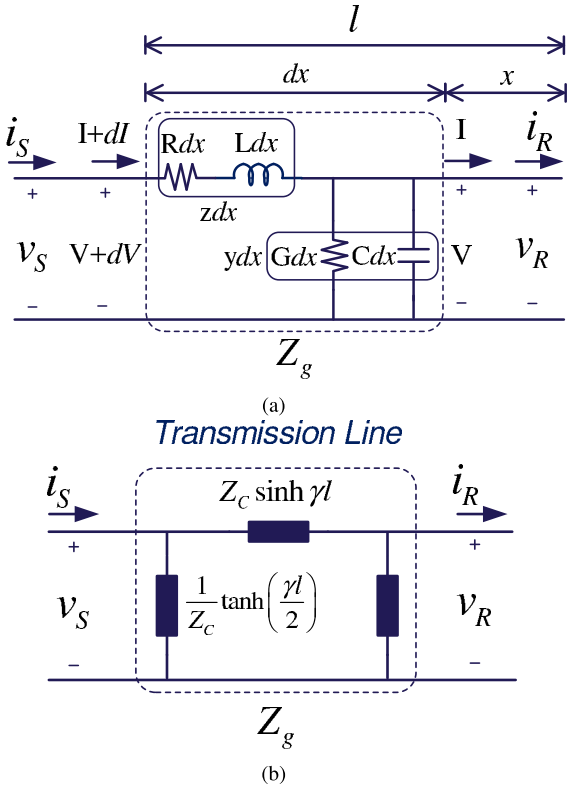

FIGURE 3. Transmission line, (a) electric circuit with distributed parameters and (b) equivalent-π model, with length l.

The circuit in Fig. 3(a) depicts the grid impedance in Fig. 1, and it shows the voltage and current relationship of the transmission line with length l and the distributed parameters, R, L, G, and C, where the V and I are the voltage and current at the distance, x, from the receiving end, v_R. Similarly, the $V + dV$ and $I + dI$ are the voltage and current at the distance, $x + dx$, from v_R [24]. The distributed parameters are defined as:

- R: Resistance along the line.
- L: Inductance along the line.
- G: Conductance shunting to the line.
- C: Capacitance shunting to the line.

where all parameters are specified in per unit length. Thus, the impedance, z, and admittance, y, per unit length can be specified as

$$z = R + j\omega L \quad y = G + j\omega C \tag{10}$$

For sinusoidal steady-state condition, applying the Kirchhoff's voltage and current laws, the differential voltage, dV, across the length, dx, and the differential current, dI, flowing into the shunt admittance in the phasor form can be derived as

$$\frac{dV}{dx} = zI \quad \frac{dI}{dx} = yV \tag{11}$$

Then, by differentiating these two first-order coupled equations, and substituting one of the equation into the other, two second-order decoupled equations are derived as

$$\frac{d^2V}{dx^2} = yzV \quad \frac{d^2I}{dx^2} = yzI \tag{12}$$

To solve these equations, the receiving end voltage and current are assumed to be known as the boundary condition. Thus, the general solutions of the voltage and current at the distance x from v_R are given as

$$\begin{aligned} V &= \frac{v_R + Z_C i_R}{2} e^{\gamma x} + \frac{v_R - Z_C i_R}{2} e^{-\gamma x} \\ I &= \frac{v_R/Z_C + i_R}{2} e^{\gamma x} - \frac{v_R/Z_C - i_R}{2} e^{-\gamma x} \end{aligned} \tag{13}$$

where Z_C and γ are called the surge impedance and the propagation constant in [24], respectively, which are shown as

$$Z_C = \sqrt{\frac{z}{y}} \quad \gamma = \sqrt{yz} \tag{14}$$

Then, the solution in (13) can be written in hyperbolic form by using the the hyperbolic constants shown below

$$\sinh \gamma x = \frac{e^{\gamma x} - e^{-\gamma x}}{2} \quad \cosh \gamma x = \frac{e^{\gamma x} + e^{-\gamma x}}{2} \tag{15}$$

where the result is shown as the two-port network representation using the transmission parameters (ABCD-parameters) given as

$$\begin{aligned} \begin{bmatrix} V \\ I \end{bmatrix} &= \begin{bmatrix} \cosh \gamma x & Z_C \sinh \gamma x \\ \dfrac{\sinh \gamma x}{Z_C} & \cosh \gamma x \end{bmatrix} \begin{bmatrix} v_R \\ -i_R \end{bmatrix} \\ &= \begin{bmatrix} A & B \\ C & D \end{bmatrix} \begin{bmatrix} v_R \\ -i_R \end{bmatrix} \end{aligned} \tag{16}$$

By letting the length $x = l$, the transmission line of the length l is then represented as the equivalent π model using the sending end voltage v_S and receiving end voltage v_R with the entering current i_S and leaving current i_R as shown in Fig. 3(b). The relationships between voltages and currents are given as

$$\begin{bmatrix} v_S \\ i_S \end{bmatrix} = \begin{bmatrix} \cosh \gamma l & Z_C \sinh \gamma l \\ \dfrac{\sinh \gamma l}{Z_C} & \cosh \gamma l \end{bmatrix} \begin{bmatrix} v_R \\ -i_R \end{bmatrix} \tag{17}$$

Since the interrelation of different parameters has already been described in the field of RF/Microwave [25], the ABCD-to-S-parameter conversion depicted in (52) in Appendix B is then applied to the transmission line model in (17), and $Z_0 = Z_C$ is selected, where the S-parameter representation of the transmission line model is derived as

$$\begin{bmatrix} \cosh \gamma l & Z_c \sinh \gamma l \\ \dfrac{\sinh \gamma l}{Z_c} & \cosh \gamma l \end{bmatrix} \overset{(52)}{\underset{Z_0 = Z_c}{\Longrightarrow}} \begin{bmatrix} 0 & e^{-\gamma l} \\ e^{-\gamma l} & 0 \end{bmatrix} \tag{18}$$

where the S-parameter representation of the transmission line model is shown as a unit delay associated with the length l and the propagation constant γ of the transmission line. To simplify the system in the following section, the transmission line is assumed lossless, i.e., $R = G = 0$, where Z_C becomes a real number representing a pure resistor and is selected as the

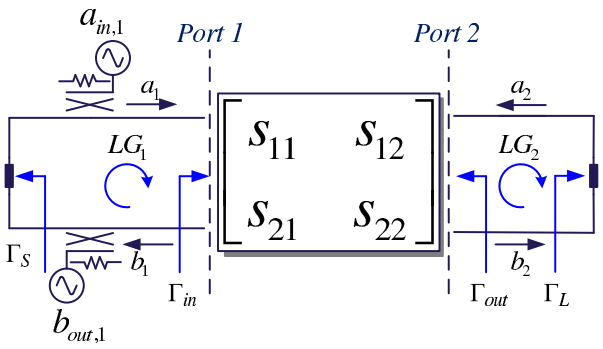

FIGURE 4. Two-port network of grid-connected VSC using S-parameters.

value of typical underground cables, 40 Ω [24], and Z_C is given as

$$Z_C = \sqrt{\frac{L}{C}} \tag{19}$$

and γ becomes an imaginary number, which describes the ideal phase delay constant given as

$$\gamma = j\omega\sqrt{LC} \tag{20}$$

Thus, the equivalent two-port network of grid-connected VSC using S-parameter can be derived in the form as (8) applying the Y-to-S-parameter conversion, which is given in (51) in Appendix A, to the existing admittance model (2) as shown in Fig. 4.

III. REFLECTION COEFFICIENT STABILITY CRITERION

To realize the stability analysis based on reflection coefficients, the derivation of SISO open-loop gain using the S-parameters and reflection coefficients is first introduced. Then, the reflection coefficient stability criterion is proposed to analyze the derived SISO open-loop gain.

A. SISO OPEN-LOOP GAIN WITH REFLECTION COEFFICIENTS

The derivation of the SISO open-loop gains with S-parameter representations and reflection coefficients has been reported in [18], in which the reflection coefficient is defined as the ratio of the reflected wave to the incident wave and is commonly expressed as Γ given as

$$\Gamma = \frac{Reflectedwave}{Incidentwave} \tag{21}$$

The source and load admittance, Y_S and Y_L in Fig. 2, can then be converted to the source and load reflection coefficients as shown in Fig. 4 as

$$\Gamma_S = \frac{\frac{1}{Y_S} - Z_0}{\frac{1}{Y_S} + Z_0} \tag{22}$$

$$\Gamma_L = \frac{\frac{1}{Y_L} - Z_0}{\frac{1}{Y_L} + Z_0} \tag{23}$$

The SISO closed-loop gain at each port is then derived by imposing a forcing wave into the network [19]. E.g., the forcing wave $a_{in,1}$ is imposed into the two-port network in Fig. 4 at Port 1, and the incident wave a_1 is derived as

$$a_1 = \Gamma_S\left(a_{in,1} + b_1\right) = \Gamma_S a_{in,1} + \Gamma_S\Gamma_{in}a_1 \tag{24}$$

The SISO closed-loop gain from $a_{in,1}$ to a_1 is then obtained as

$$\frac{a_1}{a_{in,1}} = \frac{\Gamma_S}{1 - \Gamma_S\Gamma_{in}} \tag{25}$$

where the input and output reflection coefficients, Γ_{in} and Γ_{out}, of the two-port network can be derived solving (8), (22), and (22) with algebra, or it can also be derived by simplifying the signal-flow graph (SFG), where the SFG simplification process is given in detail in Appendix C, and the results are shown as

$$\Gamma_{in} = \frac{b_1}{a_1} = S_{11} + \frac{S_{12}S_{21}\Gamma_L}{1 - S_{22}\Gamma_L} \tag{26}$$

$$\Gamma_{out} = \frac{b_2}{a_2} = S_{22} + \frac{S_{12}S_{21}\Gamma_S}{1 - S_{11}\Gamma_S} \tag{27}$$

The SISO closed-loop gain from $a_{in,1}$ to b_1 can also be derived with a similar process as (24) and is given as

$$\frac{b_1}{a_{in,1}} = \frac{\Gamma_S\Gamma_{in}}{1 - \Gamma_S\Gamma_{in}} \tag{28}$$

where the SISO open-loop gain at Port 1, LG_1, is identified both in the denominator of (25) and (28), which is equal to $-\Gamma_S\Gamma_{in}$. Similarly, the SISO open-loop gain LG_2 at Port 2 is acquired as $-\Gamma_L\Gamma_{out}$ by imposing a forcing wave at Port 2. Moreover, if the forcing wave is imposed with the direction out of the two-port network at Port 1, i.e. $b_{out,1}$, and then the SISO closed-loop gains from $b_{out,1}$ to a_1 and b_1 can be obtained as

$$\frac{a_1}{b_{out,1}} = \frac{\Gamma_S\Gamma_{in}}{1 - \Gamma_S\Gamma_{in}} \tag{29}$$

$$\frac{b_1}{b_{out,1}} = \frac{\Gamma_{in}}{1 - \Gamma_S\Gamma_{in}} \tag{30}$$

where (25), (28), (29) and (30) share the same characteristic equation, $1 - \Gamma_S\Gamma_{in}$, and the same SISO open-loop gain $-\Gamma_S\Gamma_{in}$, which means that the direction of the power wave imposed at Port 1 has no influence to the derived SISO closed- and open-loop gains.

B. REFLECTION COEFFICIENT STABILITY CRITERION

The stability of the SISO closed-loop gains, (25), (28), (29) and (30), can be analyzed by checking the existence RHP zeros in $1 - \Gamma_S\Gamma_{in}$, according to the Cauchy's argument principle [26]. To compare with the proposed reflection coefficient stability criterion with the impedance-based stability criteria, the conversion between the impedances, Z, and the reflection coefficients, Γ, are given as

$$Z = Z_0\frac{1+\Gamma}{1-\Gamma} \quad \Gamma = \frac{Z - Z_0}{Z + Z_0} \tag{31}$$

Then, the characteristic equation of the system, $1-\Gamma_S\Gamma_{in}$, can be represented with Z_S and Z_{in} by applying (31) and is given as

$$1-\Gamma_S\Gamma_{in}=\frac{2Z_0\left(Z_S+Z_{in}\right)}{\left(Z_S+Z_0\right)\left(Z_{in}+Z_0\right)} \tag{32}$$

As Z_0 is selected as a non-zero positive real number, the number of times that the trajectory $-\Gamma_S\Gamma_{in}$ clockwise encircles point $(-1,0)$ in complex plane, $\mathcal{N}_{1-\Gamma_S\Gamma_{in}}$, can then be determined as

$$\begin{aligned}\mathcal{N}_{1-\Gamma_S\Gamma_{in}}&=\mathcal{Z}\left(1-\Gamma_S\Gamma_{in}\right)-\mathcal{P}\left(1-\Gamma_S\Gamma_{in}\right)\\&=\mathcal{Z}\left(\frac{Z_S+Z_{in}}{\left(Z_S+Z_0\right)\left(Z_{in}+Z_0\right)}\right)\\&\quad-\mathcal{P}\left(\frac{Z_S+Z_{in}}{\left(Z_S+Z_0\right)\left(Z_{in}+Z_0\right)}\right)\\&=\mathcal{Z}\left(Z_S+Z_{in}\right)+\mathcal{P}\left(Z_S+Z_0\right)+\mathcal{P}\left(Z_{in}+Z_0\right)\\&\quad-\mathcal{P}\left(Z_S+Z_{in}\right)-\mathcal{Z}\left(Z_S+Z_0\right)-\mathcal{Z}\left(Z_{in}+Z_0\right)\end{aligned} \tag{33}$$

where $\mathcal{P}$ and $\mathcal{Z}$ depict the number of RHP poles and zeros, respectively. Since $\mathcal{P}\left(Z_S+Z_{in}\right)=\mathcal{P}\left(Z_S\right)+\mathcal{P}\left(Z_{in}\right)$, $\mathcal{Z}\left(1-\Gamma_S\Gamma_{in}\right)$ can then be calculated as

$$\begin{aligned}\mathcal{Z}\left(1-\Gamma_S\Gamma_{in}\right)=\mathcal{N}_{1-\Gamma_S\Gamma_{in}}&+\mathcal{P}\left(Z_S\right)+\mathcal{P}\left(Z_{in}\right)\\&+\mathcal{Z}\left(Z_S+Z_0\right)+\mathcal{Z}\left(Z_{in}+Z_0\right)\end{aligned} \tag{34}$$

which shows that $\mathcal{Z}\left(1-\Gamma_S\Gamma_{in}\right)$ is related not only the RHP open-loop poles in Z_S and Z_{in} but also the RHP closed-loop poles in Z_S+Z_0 and $Z_{in}+Z_0$. Therefore, two conditions, i.e. Z_S and Z_{in} are stable, and Z_S or Z_{in} is unstable, are discussed as follows:

1) STABLE Z_S AND Z_{in}

The impedance-based analysis has assumed that the impedances, which represent each subsystems are individually stable. With this stable subsystem assumption, the other two trajectories, $1-\Gamma_S$ and $1-\Gamma_{in}$, are needed to judge the stability. Since $\mathcal{P}\left(Z_0\right)=0$, $\mathcal{N}_{1-\Gamma_{in}}$ can be derived using (31) and shown as

$$\begin{aligned}\mathcal{N}_{1-\Gamma_{in}}&=\mathcal{Z}\left(\frac{2Z_0}{Z_{in}+Z_0}\right)-\mathcal{P}\left(\frac{2Z_0}{Z_{in}+Z_0}\right)\\&=\mathcal{P}\left(Z_{in}\right)-\mathcal{Z}\left(Z_{in}+Z_0\right)\end{aligned} \tag{35}$$

Similarly, $\mathcal{N}_{1-\Gamma_S}$ is given as

$$\mathcal{N}_{1-\Gamma_S}=\mathcal{P}\left(Z_S\right)-\mathcal{Z}\left(Z_S+Z_0\right) \tag{36}$$

Thus, $\mathcal{Z}\left(1-\Gamma_S\Gamma_{in}\right)$ in (34) is derived using (35) and (36) as

$$\begin{aligned}\mathcal{Z}\left(1-\Gamma_S\Gamma_{in}\right)=\mathcal{N}_{1-\Gamma_S\Gamma_{in}}&-\mathcal{N}_{1-\Gamma_S}-\mathcal{N}_{1-\Gamma_{in}}\\&+2\mathcal{P}\left(Z_S\right)+2\mathcal{P}\left(Z_{in}\right)\end{aligned} \tag{37}$$

With the stable subsystem assumption, which $\mathcal{P}\left(Z_S\right)=\mathcal{P}\left(Z_{in}\right)=0$, the system is stable if and only if $\mathcal{N}_{1-\Gamma_S\Gamma_{in}}-\mathcal{N}_{1-\Gamma_S}-\mathcal{N}_{1-\Gamma_{in}}=0$.

However, the stable subsystem assumption is not always applicable to the multi-bus, multi-VSC power system, since the impedance seen on a specific bus can be related to both the input impedances of VSC and the grid impedances in the system. Therefore, the unstable impedance cases need to be discussed.

2) UNSTABLE Z_S OR Z_{in}

To derive $\mathcal{Z}\left(1-\Gamma_S\Gamma_{in}\right)$ considering the unstable Z_S or Z_{in}, $\mathcal{Z}\left(1-\Gamma_S\Gamma_{in}\right)$ in (34) is reorganized using (35) and (36) and given as

$$\begin{aligned}\mathcal{Z}\left(1-\Gamma_S\Gamma_{in}\right)=\mathcal{N}_{1-\Gamma_S\Gamma_{in}}&+\mathcal{N}_{1-\Gamma_S}+\mathcal{N}_{1-\Gamma_{in}}\\&+2\mathcal{Z}\left(Z_S+Z_0\right)+2\mathcal{Z}\left(Z_{in}+Z_0\right)\end{aligned} \tag{38}$$

where (38) is then irrelevant to $\mathcal{P}\left(Z_S\right)$ and $\mathcal{P}\left(Z_{in}\right)$ unlike (37). Therefore, if $\mathcal{Z}\left(Z_S+Z_0\right)$ and $\mathcal{Z}\left(Z_{in}+Z_0\right)$ are equal to zero, the system is stable if and only if $\mathcal{N}_{1-\Gamma_S\Gamma_{in}}+\mathcal{N}_{1-\Gamma_S}+\mathcal{N}_{1-\Gamma_{in}}=0$

To let $\mathcal{Z}\left(Z_S+Z_0\right)=\mathcal{Z}\left(Z_{in}+Z_0\right)=0$, the system with the characteristic equation Z_S+Z_0 is first considered, where a closed-loop gain, G_{cl} is given as

$$G_{cl}=\frac{Z_SZ_0}{Z_S+Z_0}=\frac{Z_S}{1+\frac{1}{Z_0}Z_S} \tag{39}$$

Since G_{cl} has the form of a typical negative feedback amplifier with the pure constant negative feedback gain, $\frac{1}{Z_0}$. To analyze the stability of G_{cl} with the control theory [26], the impedance Z_S has been expressed as the ratio of two polynomials as

$$Z_S=\frac{N\left(s\right)}{D\left(s\right)} \tag{40}$$

then G_{cl} can be described as

$$G_{cl}=\frac{N\left(s\right)}{D\left(s\right)+\frac{1}{Z_0}N\left(s\right)} \tag{41}$$

where the poles of G_{cl} are given as the loot of the characteristic equation

$$D\left(s\right)+\frac{1}{Z_0}N\left(s\right)=0 \tag{42}$$

Thus, the poles of G_{cl} tend to the poles of Z_S if Z_0 tends to infinite and when Z_0 is closed to zero, the poles of G_{cl} tend to the zeros of Z_S. Accordingly, when the impedance Z_S is unstable, $\mathcal{N}_{1-\Gamma_S}$ in (36) changes with different value of Z_0. Therefore, the systems with characteristic equations Z_S+Z_0 and $Z_{in}+Z_0$ can be stabilized, whenever is possible, by properly selecting the value of Z_0, which makes $\mathcal{Z}\left(Z_S+Z_0\right)=\mathcal{Z}\left(Z_{in}+Z_0\right)=0$ [27], where the previous selected impedance 40 Ω satisfies this condition in the following case study. Thus, $\mathcal{Z}\left(1-\Gamma_S\Gamma_{in}\right)$ in (38) can be simplified as

$$\mathcal{Z}\left(1-\Gamma_S\Gamma_{in}\right)=\mathcal{N}_{1-\Gamma_S\Gamma_{in}}+\mathcal{N}_{1-\Gamma_S}+\mathcal{N}_{1-\Gamma_{in}} \tag{43}$$

where $\mathcal{N}_{1-\Gamma_S}$ and $\mathcal{N}_{1-\Gamma_{in}}$ indicate $\mathcal{P}\left(Z_S\right)$ and $\mathcal{P}\left(Z_{in}\right)$, respectively.

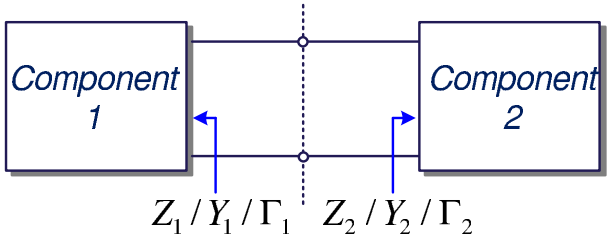

FIGURE 5. Negative-resistance model.

Consequently, the system is stable if and only if $\mathcal{N}_{1-\Gamma_S\Gamma_{in}} + \mathcal{N}_{1-\Gamma_S} + \mathcal{N}_{1-\Gamma_{in}} = 0$ with proper characteristic impedance Z_0 without the stable subsystem assumption. Moreover, the stability of Z_S and Z_{in} can be examined in the trajectory of $-\Gamma_S$ and $-\Gamma_{in}$ in the complex plane, respectively, and the relative stability indices, such as phase margin and gain margin, can be defined in the SISO open-loop gain $-\Gamma_S\Gamma_{in}$, which is superior to the impedance-based stability criteria.

C. RELATIVE STABILITY

In the marginally stable case, the SISO open-loop gain crosses exactly the critical point $(-1, 0)$, where the gain margin and phase margin occur at the same point in the Nyquist plot. Thus, the resonance frequency can be readily identified. However, when the system is barely close to marginally stable, the gain margin and phase margin exist at different frequencies, which divide the frequency response into three regions. Incorrect resonance frequency prediction may provide erroneous information, resulting in inaccurate damping solutions.

Since a passive system is undoubtedly stable, the resonance frequency of the system can be identified by the lack of passivity denoted using the negative-resistance model as shown in Fig. 5, where it is commonly used in the design of oscillators for determining the frequency at which oscillation starts in the RF/Microwave field, where the resonance condition represented with reflection coefficients has been expressed in [28] and is given as

$$\begin{aligned} &\left|\Gamma_1\left(\omega_f\right)\right| \cdot \left|\Gamma_2\left(\omega_f\right)\right| > 1 \\ &\arg\left(\Gamma_1\left(\omega_f\right)\Gamma_2\left(\omega_f\right)\right) = -180^\circ \end{aligned} \tag{44}$$

where ω_f depicts the frequency when the product of reflection coefficients on both sides is greater than 1 while the phase is equal to -180°. However, the lack of passivity is implicitly exposed in this condition. Thus, instead of directly using the reflection coefficients obtained from the SISO open-loop gains, they can be converted to the admittance form to identify the oscillating frequency utilizing the following equations [19]:

$$Y = \frac{1}{Z_0}\frac{1-\Gamma}{1+\Gamma} \tag{45}$$

Two admittances seen into the two components in Fig. 5, $Y_1 = G_1 + jB_1$ and $Y_2 = G_2 + jB_2$, are represented as the combinations of conductances and susceptances. Then the following admittance conditions can be used as the indications of circuit instability:

$$\begin{aligned} G_1\left(\omega_f\right) + G_2\left(\omega_f\right) &< 0 \\ B_1\left(\omega_f\right) + B_2\left(\omega_f\right) &= 0 \end{aligned} \tag{46}$$

where the system satisfies the negative-conductance condition when $G_1 + G_2 < 0$ while the total susceptance $B_1 + B_2$ is equal to zero, indicating 180° difference between the two components. This negative-conductance condition is regarded that the system loses its passivity, which can be used to estimate the oscillating frequency.

Therefore, even if the reflection coefficients are appropriate for judging stability and defining relative stability, the conditions depicted in admittance form of (46) are more suitable for the critically oscillating frequency identification in the multi-bus, multi-VSC power system.

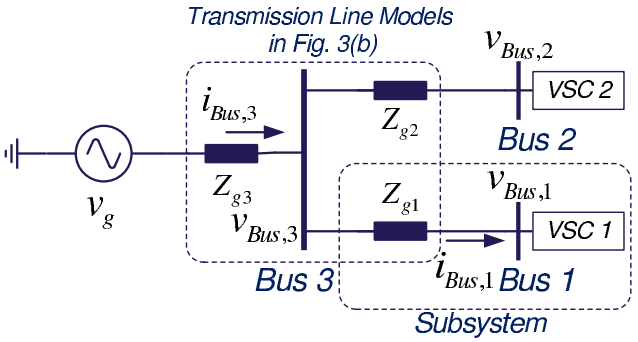

FIGURE 6. System configuration with multiple grid-connected VSCs.

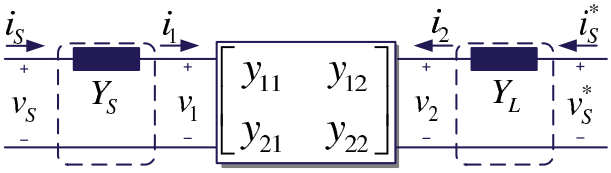

FIGURE 7. Open the circuit of the two-port network shown in Fig. 2.

IV. STABILITY ANALYSIS PROCEDURE FOR MULTI-BUS, MULTI-VSC POWER SYSTEM

To analyze the stability in the multi-bus, multi-VSC power system and further identify the potential resonance frequencies when the system is close to marginally stable, a 3-bus system with two VSCs as shown in Fig. 6 is considered, where two VSCs, VSC 1 and VSC 2, are parallel-connected at Bus 3 via two grid impedances Z_{g1} and Z_{g2}. From Bus 3, two subsystems are then connected to the ideal voltage source v_g through another grid impedance Z_{g3}. This stability analysis procedure was first briefly introduced in [20], where it is refined through the following 6 steps:

1) SELECTING A SYSTEM-SHARED CHARACTERISTIC IMPEDANCE Z_0

The selection of characteristic impedance has been discussed in Section II-B2, where the value of the surge impedance in the typical underground cables, 40 Ω, is chosen as the

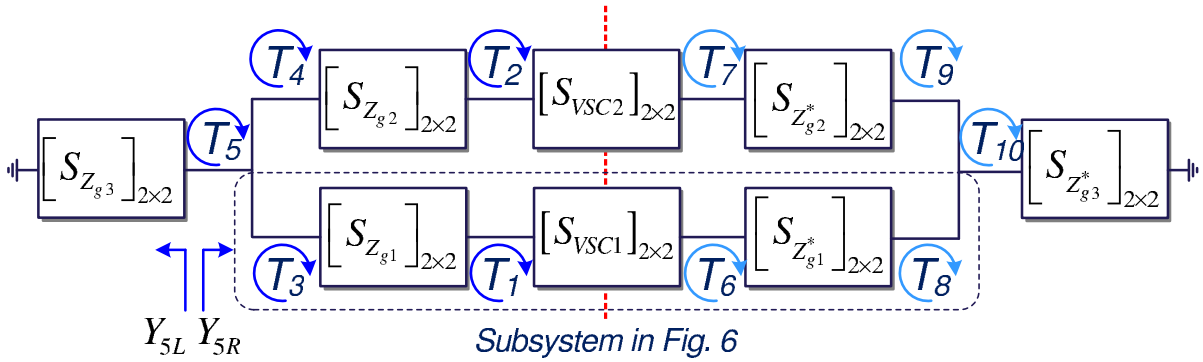

FIGURE 8. Single-line diagram of a 3-bus system shown in Fig. 6.

characteristic impedance Z_0. Since the surge impedance is determined by the geometry and materials of the transmission line, and hence it is independent of the length of the line [24].

2) ACQUIRING THE TWO-PORT NETWORK REPRESENTATIONS OF ALL COMPONENTS IN THE SYSTEM

In Fig. 6, the system includes grid impedances and VSCs. To acquire the two-port network representations, either theoretical derivations or measurement results can be employed. Firstly, consider the subsystem circled in Fig. 6, which can be seen as a single grid-connected VSC connected to the Bus 3 through one grid impedance. Thus, it can be seen as three cascaded two-port networks by opening the circuit of Fig. 2, as shown in Fig. 7. The terminated admittances Y_S and Y_L are also interpreted as two individual two-port networks, i.e. Y_S is characterized using terminal voltages v_S, v_1, and terminal current i_S, and $-i_1$.

For experimental verification, and since the characteristic impedance is independent of the line length, the short transmission line model is considered here in Fig. 7 to characterize the terminated admittances Y_S using v_S, v_1, i_S, and i_1, which the ABCD-parameters of the two-port network are given as

$$\begin{bmatrix} v_S \\ i_S \end{bmatrix} = \begin{bmatrix} A & B \\ C & D \end{bmatrix} \begin{bmatrix} v_1 \\ -i_1 \end{bmatrix} = \begin{bmatrix} 1 & \frac{1}{Y_S} \\ 0 & 1 \end{bmatrix} \begin{bmatrix} v_1 \\ -i_1 \end{bmatrix} \tag{47}$$

where the two-port network representation of the load admittance Y_L can be similarly derived using v_S^*, v_2, i_S^*, and i_2 as

$$\begin{bmatrix} v_S^* \\ i_S^* \end{bmatrix} = \begin{bmatrix} 1 & \frac{1}{Y_L} \\ 0 & 1 \end{bmatrix} \begin{bmatrix} v_2 \\ -i_2 \end{bmatrix} \tag{48}$$

3) APPLYING THE CONVERSIONS BETWEEN S-PARAMETERS AND OTHER ELECTRICAL PARAMETERS

The Y-to-S-parameter and ABCD-to-S-parameter conversions have been specified in [25] and are also given in Appendix A and B. With Z_0 selected above, the system depicted in Fig. 6 is then represented as two-port networks connections as shown in Fig. 8.

4) DERIVING THE SISO OPEN-LOOP GAINS ON EACH BUS

To derive the SISO open-loop gain on a particular bus in Fig. 8, the reflection coefficients on both sides of the bus need to be acquired. Since all the networks in the system are two-port network representations, the reflection coefficient can be derived by realizing the SFG reduction process depicted in Appendix C. However, the reflection coefficients have already been adopted in the field of RF/Microwave circuit design for decades, and the analytic equations of the reflection coefficients is highly dependent on the connection of the networks in the system. In this paper, the reflection coefficients in the validation are derived with the help of computer-aided software, NI AWR Design Environment™ [29], where the measurement devices, Gamma probe (GPROBE2) [30], are used to derive the reflection coefficients and the SISO open-loop gains on each bus, and the results are plotted in the Nyquist plots.

5) IDENTIFYING THE SENSITIVE SISO OPEN-LOOP GAIN

The sensitive bus has the minimum phase and/or gain margins, which also indicates the location of the potential instability in the system. The SISO open-loop gains T_1 to T_{10} as shown in Fig. 8 are examined to analyze the stability of the system with the proposed reflection coefficient stability criterion. Nevertheless, since the frequency response of the open-loop gains on both sides of the red dashed line in Fig. 8 are just frequency-shifted with two times the fundamental frequency, the system stability can be analyzed by deriving five open-loop gains from T_1 to T_5 first, and then checking the sensitive SISO open-loop gain pair, e.g. (T_5, T_{10}), to capture the frequency coupling phenomenon.

6) CONVERTING THE REFLECTION COEFFICIENTS TO ADMITTANCES AND EXAMINING THE RESONANCE CONDITION

The reflection coefficients at the sensitive bus, which form the critical SISO open-loop gain, are converted to the admittance form using (45) and then use the resonance condition

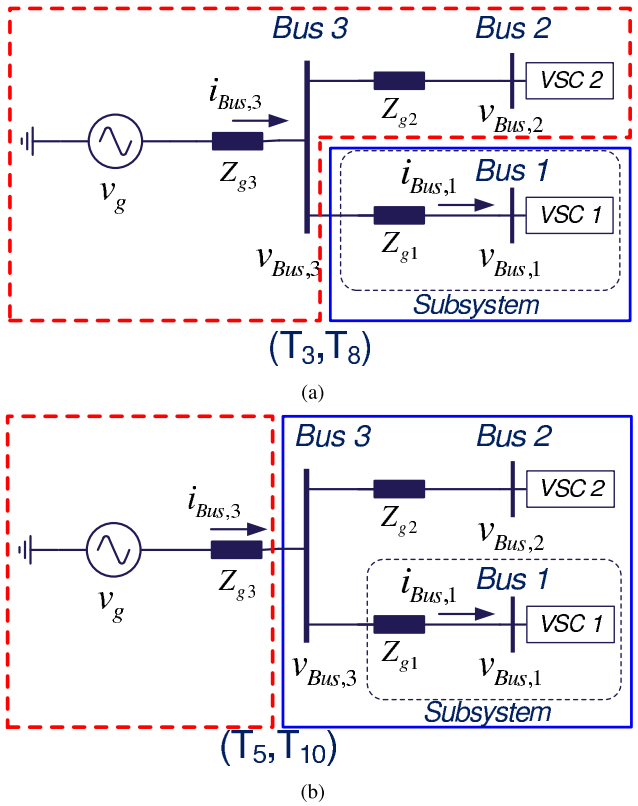

FIGURE 9. SISO open-loop gain pairs, (a) (T_3, T_8) and (b) (T_5, T_{10}), depicted in Fig. 8.

specified in (46) to identify the critically oscillating frequency. It is worthwhile to mention that there are multiple SISO open-loop gain pairs at Bus 3, which are (T_3, T_8), (T_4, T_9), and (T_5, T_{10}), representing different open-loop gains of similar components. Fig. 9(a) shows the SISO open-loop gains pair (T_3, T_8) depicted in Fig. 8, where the reflection coefficient encircled with blue solid line contains the VSC 1 in series with the grid impedance Z_{g1}, and the reflection coefficient encircled with red dashed line is composed of the contribution of VSC 2 in series with the grid impedance Z_{g2} and paralleled with Z_{g3}. On the other hand, the SISO open-loop gains pair (T_5, T_{10}) as shown in Fig. 9(b) contains also two parts. The reflection coefficient encircled with blue solid line is the contribution of the paralleled connection of two VSC subsystems, and the reflection coefficient encircled by the red dashed line only contains the grid impedance Z_{g3}.

These different SISO open-loop gain pairs share the same bus but have different physical implications, which distinguishes the contributions of the components in the system.

V. CASE STUDIES WITH EXPERIMENTAL VERIFICATION

To validate the effectiveness of the theoretical analysis, the system depicted in Fig. 6 is used to perform case studies based on the theoretically derived open-loop gains. The grid impedances Z_{g1}, Z_{g2}, and Z_{g3} are implemented with three-phase ac inductors, where Z_{g1} and Z_{g2} are 4 mH inductors and Z_{g3} is an 11 mH inductor in the experimental test.

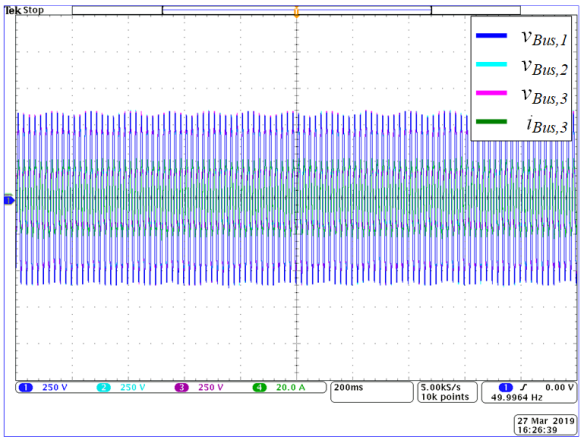

(a) Voltage waveforms on each bus and the total output current (X-axis: 200 ms/div, Y-axis: $v_{Bus,1}$, $v_{Bus,2}$, $v_{Bus,3}$: 250 V/div, $i_{Bus,3}$: 20 A/div).

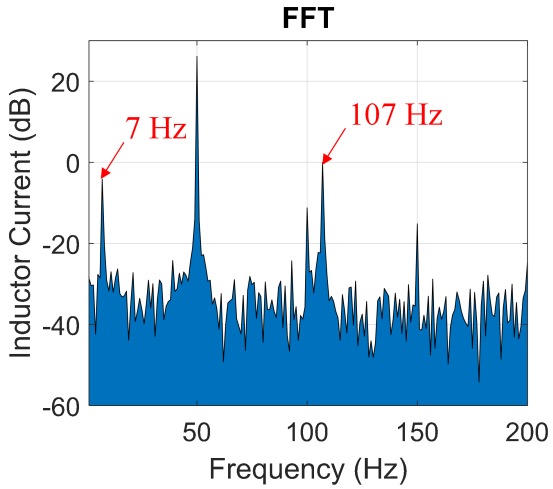

(b) Frequency spectrum of the current $i_{Bus,3}$ in Fig. 10(a)

FIGURE 10. Experimental results with the system parameters given in TABLE 1, and system shown in Fig. 6.

For the VSCs in Fig. 6, two stiff dc voltage sources are individually connected to the dc side of VSC 1 and VSC 2 to prevent any influence of dc bus voltage control (Fig. 6). Thus, only the digital current controller in the dq-frame and the PLL are considered, and two VSCs have the same current controller parameters and the same active power output P_{out}, but different PLL parameters.

In the PLLs, the PI controllers are utilized to synchronize with the grid voltage, where the proportional gains $K_{pp,1}$ and $K_{pp,2}$ are set with the same value, 1 rad s^{-1} V^{-1}, but the integral gains in the PLL, $K_{pi,1}$ and $K_{pi,2}$, are set to have different values. The parameters used in the experiment and the theoretical validations are listed in TABLE 1.

Fig. 10(a) shows the measured voltage waveforms on each bus, $v_{Bus,1}$, $v_{Bus,2}$, $v_{Bus,3}$, and the total output current $i_{Bus,3}$ as depicted in Fig. 6 using the listed parameters. The system starts to resonate and two resonance frequencies, 7 Hz and 107 Hz, are identified in the frequency spectra of the current, as shown in Fig. 10(b). To theoretically validate the experimental result, the small-signal admittance matrix of the

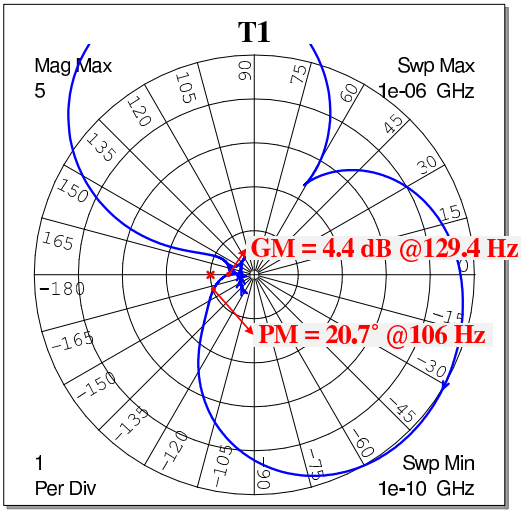

(a) Open-loop gain T_1

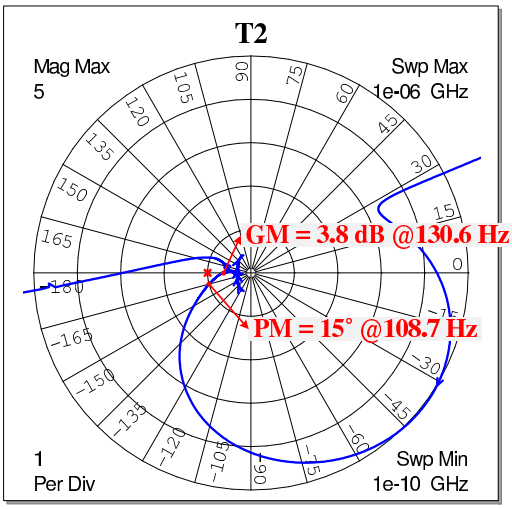

(b) Open-loop gain T_2

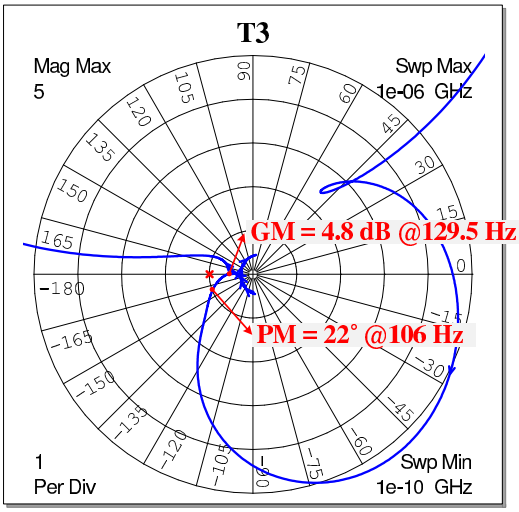

(c) Open-loop gain T_3

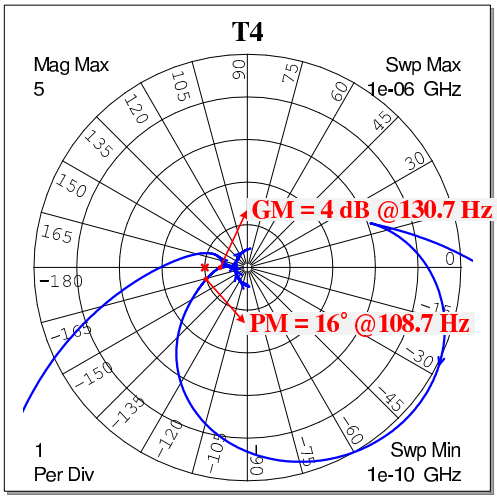

(d) Open-loop gain T_4

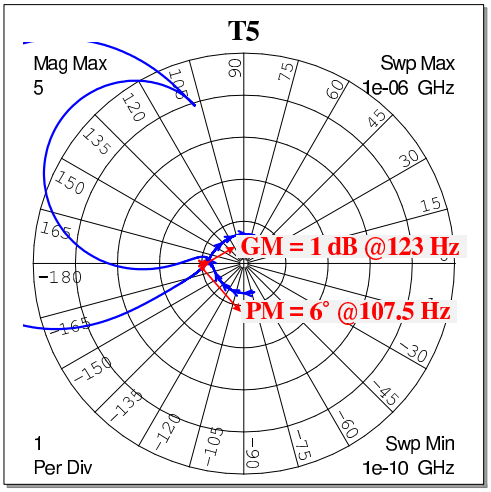

(e) Open-loop gain T_5

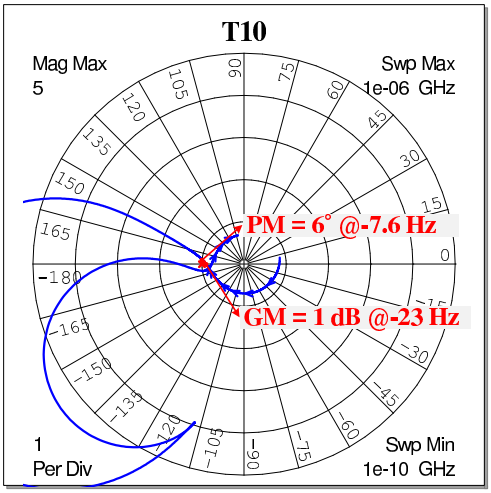

(f) Open-loop gain T_{10}

FIGURE 11. Open-loop gains of the model depicted in Fig 8 and circuit in Fig. 6 using the parameters listed in Fig. 1 using NI AWR Design Environment™.

TABLE 1. Parameters used in experiment and case studies.

System symbol	Parameter Description	Value
v_g	Grid voltage	400 V_{rms}
P_{out}	Output power of each VSCs	5.5 kW
Z_{g1}, Z_{g2}	Grid impedances Z_{g1} and Z_{g2}	4 mH
Z_{g3}	Grid impedance Z_{g3}	11 mH
$K_{pp,1}, K_{pp,2}$	Proportional gain in each PLLs	1 $\mathrm{rad\,s^{-1}\,V^{-1}}$
$K_{pi,1}$	Integral gain in PLL of VSC 1	100 $\mathrm{rad\,s^{-2}\,V^{-1}}$
$K_{pi,2}$	Integral gain in PLL of VSC 2	253 $\mathrm{rad\,s^{-2}\,V^{-1}}$

TABLE 2. Gain and phase margin in each open-loop gain.

Open-loop gain	Gain margin	Phase margin
T_1	4.4 dB@129.4 Hz	20.7°@106 Hz
T_2	3.8 dB@130.6 Hz	15°@108.7 Hz
T_3	4.8 dB@129.5 Hz	22°@106 Hz
T_4	4 dB@130.7 Hz	16°@108.7 Hz
T_5	1 dB@123 Hz	6°@107.5 Hz
T_{10}	1 dB@-23 Hz	6°@-7.6 Hz

VSC in [8] is adopted, where the frequency response data but not the transfer function matrix is used and is converted to an S-parameter representation with 40 Ω characteristic impedance. Similarly, the grid impedances Z_{g1}, Z_{g2}, Z_{g3}, and their complex conjugates are also converted to the S-parameter representations. The gamma probe GPROBE2 element in the NI AWR Design Environment™, is then used to obtain the open-loop gain at each bus and the results are plotted in the Nyquist plots as shown in Fig. 11.

To compare each open-loop gain and analyze the stability of the whole system, the critical points $(-1, 0)$ are indicated by the red cross. The gain margin and phase margin of each open-loop gain are listed in TABLE 2. Fig. 11(a) shows the open-loop gain T_1 at Bus 1, which is close to VSC 1 but far from VSC 2. The gain margin is 4.4 dB (at frequency of 129.4 Hz) and phase margin is 20.7° (at frequency of 106 Hz). For comparison, Fig. 11(b) shows the open-loop gain T_2 at Bus 2, which is close to VSC 2 but far from VSC 1 and the gain margin is 3.8 dB (at frequency of 130.6 Hz) and phase margin is 15° (at frequency of 108.7 Hz). Since the integral gain of the PLL in VSC 2 has a higher value than the one used in VSC 1, a smaller stability margin in the open-loop gain T_2 is expected. However, neither T_1 nor T_2 is the most critical open-loop gain in the system. Instead, the open-loop gain T_5 at Bus 3 has the lowest gain margin 1 dB (at frequency of 123 Hz) and the lowest phase margin 6° (at frequency of 107.5 Hz) in the whole system. Thus, when the system is marginally stable, the resonance occurs at Bus 3 and then propagates to other buses, which destabilizes the whole system.

As shown in Fig. 10(b), there are two resonance frequencies at 7 Hz and 107 Hz, where the resonance at

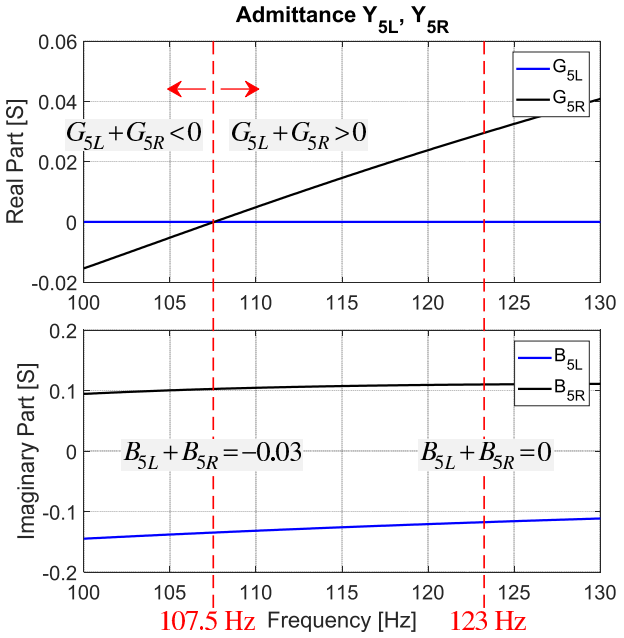

FIGURE 12. Admittance Y_{5L} and Y_{5R} shown in Fig 8 of the system shown in Fig. 6.

107 Hz is identified in Fig. 11(e). To capture the other coupling frequency 7 Hz, the open-loop gain T_{10} shown in Fig. 11(f) is inspected, which has 1 dB gain margin (at frequency of −23 Hz) and the phase margin is is 6° (at frequency of −7.6 Hz). The critical frequency appears at the negative frequency, which implies a negative-sequence resonant component in the three-phase system, yet the frequency spectra in Fig. 10(b) cannot reveal the sequence information.

In the open-loop gain T_5 on Bus 3, The gain margin is shown at 123 Hz, and the phase margin is shown at 107.5 Hz. To identify the resonance frequency, the admittances Y_{5L} and Y_{5R} in Fig. 8 are derived from the measured reflection coefficients using (45) as shown in Fig 12. The admittance Y_{5L} is composed by grid impedance Z_{g3}, and thus the conductance G_{5L} remains zero and the susceptance B_{5L} increases as the frequency increases. In contrast, the admittance Y_{5R} is contributed mainly by the dynamics of VSCs, and the conductance G_{5R} becomes negative below 107.5 Hz. The negative-conductance condition is fulfilled on Bus 3 when

the frequency is below 107.5 Hz, even if the summation of susceptance is equal to −0.03 S but not zero at 107.5 Hz, this resonance is still stimulated.

VI. CONCLUSION

In this paper, a SISO reflection coefficient stability criterion has been proposed, which simultaneously has two remarkable properties over the impedance-based stability criteria: 1) There is no prerequisite for the subsystem to be stable, i.e., the impedances derived from a specific bus can have RHP poles. 2) The relative stability can be defined at each bus for system design. Based on this stability criterion and based on the S-parameters and reflection coefficients modeling method, a system stability analysis procedure has then been suggested for modeling and analyzing the multi-bus, multi-VSC power systems. In the case study, the SISO open-loop gains on each bus have been individually derived and analyzed with proposed stability criterion, where the stability margins can be readily determined and the sensitive bus can be identified. Furthermore, the potential resonance frequency can also be explicitly indicated by investigating the passivity of the system. Experimental results have confirmed the effectiveness of the approach and the findings.

APPENDIX A
Y-TO-S CONVERSION

The relationships between various common two-port parameters, Z-, Y-, G-, H-, ABCD-, and S-parameters have been reported in the field of RF/Microwave [25]. Two key conversions used in this paper are listed here for readers' references. Assume the characteristic impedances Z_0 of each ports is identical. The real part of Z_0 is given as

$$Re\{Z_0\} = \frac{Z_0 + Z_0^*}{2} \tag{49}$$

where Z_0^* is the complex conjugate of Z_0. By rearranging (7), the terminal voltage and current are described using the power waves, a_1 and b_1, as

$$\begin{aligned} v_i &= \sqrt{\frac{2}{Z_0 + Z_0^*}} \cdot \left(Z_0^* a_i + Z_0 b_i\right) \\ i_i &= \sqrt{\frac{2}{Z_0 + Z_0^*}} \cdot (a_i - b_i), \quad i = 1, 2 \end{aligned} \tag{50}$$

To derive the expressions for S-parameters in terms of the Y-parameters, substitute (50) into (2) to solve for b_1 and b_2 in the form of (8). The results are given as

$$\begin{aligned} s_{11} &= \frac{(1 - Z_0 y_{11})(1 + Z_0 y_{22}) + Z_0^2 y_{12} y_{21}}{(1 + Z_0 y_{11})(1 + Z_0 y_{22}) - Z_0^2 y_{12} y_{21}} \\ s_{12} &= \frac{-2 Z_0 y_{12}}{(1 + Z_0 y_{11})(1 + Z_0 y_{22}) - Z_0^2 y_{12} y_{21}} \\ s_{21} &= \frac{-2 Z_0 y_{21}}{(1 + Z_0 y_{11})(1 + Z_0 y_{22}) - Z_0^2 y_{12} y_{21}} \\ s_{11} &= \frac{(1 + Z_0 y_{11})(1 - Z_0 y_{22}) + Z_0^2 y_{12} y_{21}}{(1 + Z_0 y_{11})(1 + Z_0 y_{22}) - Z_0^2 y_{12} y_{21}} \end{aligned} \tag{51}$$

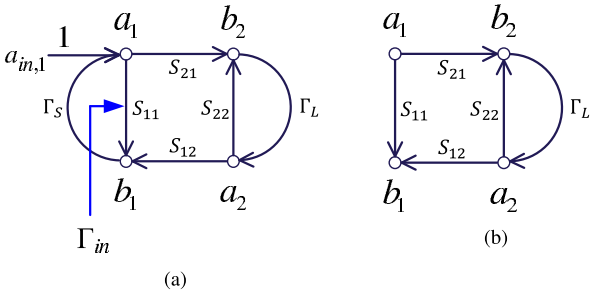

FIGURE 13. (a) SFG of Fig. 4 and (b) SFG considering a_1 in Fig. 4 as an independent node.

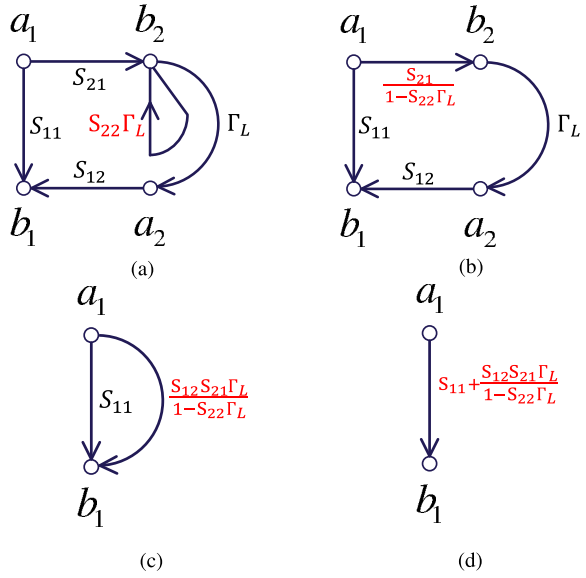

FIGURE 14. SFG reduction process (a) Step 1 (b) Step 2 (c) Step 3 and (d) Step 4.

APPENDIX B
ABCD-TO-S CONVERSION

For acquiring the expression for S-parameters in terms of the ABCD-parameters, A similar process to Appendix A is employed, which substitutes (50) into (47) to solve for b_1 and b_2 in the form of (8), and the relationships are given as

$$\begin{aligned} s_{11} &= \frac{A + B/Z_0 - CZ_0 - D}{A + B/Z_0 + CZ_0 + D} \\ s_{12} &= \frac{2(AD - BC)}{A + B/Z_0 + CZ_0 + D} \\ s_{21} &= \frac{2}{A + B/Z_0 + CZ_0 + D} \\ s_{22} &= \frac{-A + B/Z_0 - CZ_0 + D}{A + B/Z_0 + CZ_0 + D} \end{aligned} \tag{52}$$

APPENDIX C
SIGNAL-FLOW GRAPH REDUCTION

Signal-flow graph (SFG) is a graphical tool used for reducing complex network, and it provides a systematic approach to simplifying networks, where the properties of SFG have been reported in 50s [31], [32]. To demonstrate the SFG reduction

process, the circuit in Fig. 4 is used as an example, where the SFG of the circuit is given in Fig. 13(a). To derive the input reflection coefficient Γ_{in}, which is equal to $\frac{b_1}{a_1}$, a_1 needs to be set as an independent node, which has no incoming branches, shown in Fig. 13(b).

The SFG reduction can be achieved applying the transformations in [31] by following steps:

Step 1: Apply star-to-mesh equivalence on node a_2, the circuit in Fig. 14(a) can be derived.

Step 2: The self-loop in Fig. 14(a) can be eliminated by applying self-loop-to-branch transformation on node b_2. The circuit in Fig. 14(b) is then derived.

Step 3: The $a_1-b_2-a_2-b_1$ branch can be simplified using cascade transformation, where the result is shown in Fig. 14(c).

Step 4: The circuit in Fig. 14(c) is then simplified using parallel transformation, where the input reflection coefficient Γ_{in} is finally derived as (26) in Fig. 14(d).

REFERENCES

[1] F. Blaabjerg, Y. Yang, D. Yang, and X. Wang, "Distributed power-generation systems and protection," *Proc. IEEE*, vol. 105, no. 7, pp. 1311–1331, Jul. 2017.

[2] X. Wang, F. Blaabjerg, and W. Wu, "Modeling and analysis of harmonic stability in an AC power-electronics-based power system," *IEEE Trans. Power Electron.*, vol. 29, no. 12, pp. 6421–6432, Dec. 2014.

[3] X. Wang and F. Blaabjerg, "Harmonic stability in power electronic-based power systems: Concept, modeling, and analysis," *IEEE Trans. Smart Grid*, vol. 10, no. 3, pp. 2858–2870, May 2019.

[4] L. Harnefors, M. Bongiorno, and S. Lundberg, "Input-admittance calculation and shaping for controlled voltage-source converters," *IEEE Trans. Ind. Electron.*, vol. 54, no. 6, pp. 3323–3334, Dec. 2007.

[5] B. Wen, D. Boroyevich, R. Burgos, P. Mattavelli, and Z. Shen, "Analysis of D-Q small-signal impedance of grid-tied inverters," *IEEE Trans. Power Electron.*, vol. 31, no. 1, pp. 675–687, Jan. 2016.

[6] A. Rygg, M. Molinas, C. Zhang, and X. Cai, "A modified sequence-domain impedance definition and its equivalence to the dq-domain impedance definition for the stability analysis of AC power electronic systems," *IEEE J. Emerg. Sel. Topics Power Electron.*, vol. 4, no. 4, pp. 1383–1396, Dec. 2016.

[7] M. Cespedes and J. Sun, "Impedance modeling and analysis of grid-connected voltage-source converters," *IEEE Trans. Power Electron.*, vol. 29, no. 3, pp. 1254–1261, Mar. 2014.

[8] X. Wang, L. Harnefors, and F. Blaabjerg, "Unified impedance model of grid-connected voltage-source converters," *IEEE Trans. Power Electron.*, vol. 33, no. 2, pp. 1775–1787, Feb. 2018.

[9] M. K. Bakhshizadeh, X. Wang, F. Blaabjerg, J. Hjerrild, Ł. Kocewiak, C. L. Bak, and B. Hesselbæk, "Couplings in phase domain impedance modeling of grid-connected converters," *IEEE Trans. Power Electron.*, vol. 31, no. 10, pp. 6792–6796, Oct. 2016.

[10] D. Lu, X. Wang, and F. Blaabjerg, "Impedance-based analysis of DC-link voltage dynamics in voltage-source converters," *IEEE Trans. Power Electron.*, vol. 34, no. 4, pp. 3973–3985, Apr. 2019.

[11] B. Wen, D. Boroyevich, R. Burgos, P. Mattavelli, and Z. Shen, "Small-signal stability analysis of three-phase AC systems in the presence of constant power loads based on measured d-q frame impedances," *IEEE Trans. Power Electron.*, vol. 30, no. 10, pp. 5952–5963, Oct. 2015.

[12] H. Zhang, X. Wang, L. Harnefors, H. Gong, J.-P. Hasler, and H.-P. Nee, "SISO transfer functions for stability analysis of grid-connected voltage-source converters," *IEEE Trans. Ind. Appl.*, vol. 55, no. 3, pp. 2931–2941, May/Jun. 2019.

[13] L. Harnefors, "Modeling of three-phase dynamic systems using complex transfer functions and transfer matrices," *IEEE Trans. Ind. Electron.*, vol. 54, no. 4, pp. 2239–2248, Aug. 2007.

[14] S.-F. Chou, X. Wang, and F. Blaabjerg, "Two-port network modeling and stability analysis of grid-connected current-controlled VSCs," *IEEE Trans. Power Electron.*, vol. 35, no. 4, pp. 3519–3529, Apr. 2020.

[15] F. Liu, J. Liu, H. Zhang, and D. Xue, "Stability issues of $Z + Z$ type cascade system in hybrid energy storage system (HESS)," *IEEE Trans. Power Electron.*, vol. 29, no. 11, pp. 5846–5859, Nov. 2014.

[16] X. Wang, F. Blaabjerg, and P. C. Loh, "An impedance-based stability analysis method for paralleled voltage source converters," in *Proc. Int. Power Electron. Conf. (IPEC-Hiroshima-ECCE ASIA)*, May 2014, pp. 1529–1535.

[17] H. Liu, X. Xie, X. Gao, H. Liu, and Y. Li, "Stability analysis of SSR in multiple wind farms connected to series-compensated systems using impedance network model," *IEEE Trans. Power Syst.*, vol. 33, no. 3, pp. 3118–3128, May 2018.

[18] S.-F. Chou, X. Wang, and F. Blaabjerg, "Extensions to two-port network modeling method and analysis of multiple-VSC-based systems," in *Proc. 20th Workshop Control Modeling Power Electron. (COMPEL)*, Jun. 2019, pp. 1–8.

[19] R. Gilmore and L. Besser, *Practical RF Circuit Design for Modern Wireless Systems: Active Circuits and Systems* (Active Circuits and Systems). Norwood, MA, USA: Artech House, 2003.

[20] S.-F. Chou, X. Wang, and F. Blaabjerg, "Stability analysis of grid-connected VSCs based on S-parameters and reflection coefficient," in *Proc. IEEE Energy Convers. Congr. Expo. (ECCE)*, Sep. 2019, pp. 5171–5178.

[21] W. Chen, *Active Network Analysis* (Advanced Series in Electrical and Computer Engineering). Singapore: World Scientific, 1991.

[22] K. Kurokawa, "Power waves and the scattering matrix," *IEEE Trans. Microw. Theory Techn.*, vol. MTT-13, no. 2, pp. 194–202, Mar. 1965.

[23] L. Besser and R. Gilmore, *Practical RF Circuit Design for Modern Wireless Systems: Passive Circuits and Systems Passive Circuits and Systems* (Artech House Microwave Library), vol. 1. Norwood, MA, USA: Artech House, 2002.

[24] P. Kundur, *Power System Stability and Control*. New York, NY, USA: McGrawHill, 1994.

[25] D. A. Frickey, "Conversions between S, Z, Y, H, ABCD, and T parameters which are valid for complex source and load impedances," *IEEE Trans. Microw. Theory Techn.*, vol. 42, no. 2, pp. 205–211, Feb. 1994.

[26] R. Dorf and R. Bishop, *Modern Control Systems*. London, U.K.: Pearson, 2011.

[27] S. Skogestad and I. Postlethwaite, *Multivariable Feedback Control: Analysis and Design*. Hoboken, NJ, USA: Wiley, 2005.

[28] N. M. Nguyen and R. G. Meyer, "Start-up and frequency stability in high-frequency oscillators," *IEEE J. Solid-State Circuits*, vol. 27, no. 5, pp. 810–820, May 1992.

[29] AWR, Inc. *NI AWR Design Environment, V14*. Accessed: May 4, 2020. [Online]. Available: https://www.awrcorp.com/

[30] C. Campbell and S. Brown, "Modified S-probe circuit element for stability analysis," *AWR Microw. Office Manual*, 1995. [Online]. Available: http://kb.awr.com/display/help/Modified+S-Probe+Circuit+Element+for+Stability+Analysis

[31] S. Mason, "Feedback theory-some properties of signal flow graphs," *Proc. IRE*, vol. 41, no. 9, pp. 1144–1156, Sep. 1953.

[32] S. Mason, "Feedback theory-further properties of signal flow graphs," *Proc. IRE*, vol. 44, no. 7, pp. 920–926, Jul. 1956.

SHIH-FENG CHOU (Member, IEEE) received the B.S. and M.S. degrees in electrical engineering from National Tsing Hua University, Hsinchu, Taiwan, in 2009 and 2011, respectively. He is currently pursuing the Ph.D. degree with Aalborg University, Aalborg, Denmark.

He had performed Research and Development in power electronics for renewable energy systems with Delta Electronics Inc., Taoyuan, Taiwan, from 2012 to 2017. Since 2017, he has been a Research Assistant with the Department of Energy Technology, Aalborg University. His research interest includes modeling of large-scale power electronics-based power systems.

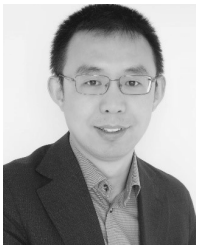

XIONGFEI WANG (Senior Member, IEEE) received the B.S. degree in electrical engineering from Yanshan University, Qinhuangdao, China, in 2006, the M.S. degree in electrical engineering from the Harbin Institute of Technology, Harbin, China, in 2008, and the Ph.D. degree in energy technology from Aalborg University, Aalborg, Denmark, in 2013.

Since 2009, he has been with the Department of Energy Technology, Aalborg University, where he was an Assistant Professor, in 2014, an Associate Professor, in 2016, a Professor and Research Program Leader for Electronic Power Grid (eGrid), in 2018, and the Director of the Aalborg University-Huawei Energy Innovation Center, in 2020. His current research interests include modeling and control of grid-interactive power converters, stability and power quality of converter-based power systems, and active and passive filters.

Dr. Wang was selected into Aalborg University Strategic Talent Management Program, in 2016. He has received the six IEEE Prize Paper Awards, the 2016 Outstanding Reviewer Award of the IEEE Transactions on Power Electronics, the 2018 IEEE PELS Richard M. Bass Outstanding Young Power Electronics Engineer Award, the 2019 IEEE PELS Sustainable Energy Systems Technical Achievement Award, and the 2019 Highly Cited Researcher by Clarivate Analytics (former Thomson Reuters). He serves as a Member at Large for Administrative Committee of the IEEE Power Electronics Society, in 2020–2022. He serves as an Associate Editor for the IEEE TRANSACTIONS ON POWER ELECTRONICS, the IEEE TRANSACTIONS ON INDUSTRY APPLICATIONS, and the IEEE JOURNAL OF EMERGING AND SELECTED TOPICS IN POWER ELECTRONICS.

FREDE BLAABJERG (Fellow, IEEE) received the Ph.D. degree in electrical engineering from Aalborg University, in 1995, and the Honoris Causa from the University Politehnica Timisoara (UPT), Romania, and Tallinn Technical University (TTU), Estonia.

From 1987 to 1988, he was with ABB-Scandia, Randers, Denmark. He was an Assistant Professor, in 1992, an Associate Professor, in 1996, and a Full Professor of power electronics and drives, in 1998. Since 2017, he has been a Villum Investigator. He has published more than 600 journal articles in the fields of power electronics and its applications. He is the coauthor of four monographs. His current research interests include power electronics and its applications, such as in wind turbines, PV systems, reliability, harmonics, and adjustable speed drives.

Dr. Blaabjerg has received 31 the IEEE Prize Paper Awards, the IEEE PELS Distinguished Service Award, in 2009, the EPE-PEMC Council Award, in 2010, the IEEE William E. Newell Power Electronics Award 2014, the Villum Kann Rasmussen Research Award 2014, and the Global Energy Prize, in 2019. He serves as the President of the IEEE Power Electronics Society, during 2019–2020. He is the Vice-President of the Danish Academy of Technical Sciences. From 2006 to 2012, he was the Editor-in-Chief of the IEEE TRANSACTIONS ON POWER ELECTRONICS. He is an editor of ten books in power electronics and its applications. From 2005 to 2007, he was a Distinguished Lecturer for the IEEE Power Electronics Society and the IEEE Industry Applications Society, from 2010 to 2011, as well as from 2017 to 2018. He is nominated in 2014–2019 by Thomson Reuters to be between the most 250 cited researchers in Engineering in the world.